ARTICLE

Received 00th January 20xx,
Accepted 00th January 20xx

DOI: 10.1039/x0xx00000x

Phosphine Vapor-assisted Construction of Heterostructured $Ni_2P/NiTe_2$ Catalysts for Efficient Hydrogen Evolution

Yibing Li,[a] Xin Tan,[b] Hao Tan,[c] Hangjuan Ren,[a] Sheng Chen,[a] Wanfeng Yang,[a] Sean C. Smith[b] and Chuan Zhao*[a]

Heterostructured catalysts with unique interfaces and properties endow distinct advantages for many electrochemical reactions. Herein, a phosphine (PH_3) vapor-assisted phase and structure engineering strategy is developed for the controllable conversion of non-active NiTe into a heterostructured active $Ni_2P/NiTe_2$ catalyst for alkaline hydrogen evolution reaction (HER). The crystalline $NiTe_2$ phase in-situ generated in a PH_3 vapor environment and the nanosheet morphology both contribute to the outstanding alkaline HER performance with an overpotential only of 62 mV to achieve a current density of -10 mA cm^{-2}. Experimental and DFT mechanistic studies suggest the $Ni_2P/NiTe_2$ interfaces provide abundant exposed active sites. The $Ni_2P/NiTe_2$ catalyst shows the lowest kinetic barrier for water dissociation and the adsorbed H* can simultaneously bind to two Ni atoms at the interface of $Ni_2P/NiTe_2$(011), which greatly enhances the H* binding and HER activities. DFT simulation also shows that more electrons transfer from Ni atoms to H* on $Ni_2P/NiTe_2$(011) (0.22 e^-) compared to that on $NiTe_2$(011) (0.13 e^-), which can explain the enhanced H* binding at the $Ni_2P/NiTe_2$(011) interface. The PH_3 vapor synthetic approach is also applied to treat chalcogenide-based materials with low HER activities, such as Ni_3S_2, to create Ni_2P/NiS_2 interfaces with significantly enhanced HER activity.

1 Introduction

Hydrogen (H_2) as a clean carbon-free energy carrier has been considered as a promising alternative to fossil fuels[1]. Hydrogen evolution reaction (HER) from water electrolysis using renewable electricity from solar and wind has been regarded as one of the most sustainable ways for efficient production of high purity H_2[2, 3]. Pt is the benchmark catalyst for HER[4-6], but its practical application is greatly limited by the scarcity and high cost. Thus, developing earth-abundant catalysts with high electrocatalytic activity for HER is one of the top priorities to enable the H_2 economy. To date, various earth-abundant catalysts with considerable HER activity have been reported. Among them, transition-metal-based sulphides[7], selenides[8] and nitrides[9] have been widely investigated. Recently, a number of heterostructured materials have also been studied for electrochemical applications[10, 11]. Particularly, van der Waals layered heterostructured materials can offer the large exposure of active sites, increased contact area with electrolyte, and improved kinetics of ion transfer for water splitting. For example, various heterostructured catalysts based on metal dichalcogenides, such as $MoS_2/Co(OH)_2$[12] $CoSe_2/MoSe_2$[13], $MoSe_2/NiSe$[14], and $NiCo_2S_4/Ni_3S_2$[15] have been reported to show extraordinary catalytic performance toward electrochemical water splitting over their counterparts. However, tellurium has rarely been combined with transition metals to form heterostructures for HER[16]. The key challenge is the common hypothesis of large Gibbs free energies of hydrogen adsorption at the metallic telluride surface that are unfavorable for HER.

In addition to the effect of heterostructures, the specific crystalline phase of a catalyst also plays a significant role for electrochemical water splitting. For example, it is reported $NiSe_2$ is catalytically more active for HER than Ni_3Se_2[17], due to the similar *d*-band electronic structure of $NiSe_2$ to Pt with optimal H intermediate adsorption energies[18, 19]. Furthermore, owing to the high electrical conductivity, metallic 1T MoS_2 is more desirable than semiconductor 2H MoS_2 for catalyzing electrochemical H_2 production from water[20]. Thus, fabrication of catalysts with controlled growth of active crystalline phase for water electrolysis is highly important.

In this study, we show a facile PH_3 vapor-assisted approach for the fabrication of $Ni_2P/NiTe_2$ heterostructures with tunable phase and morphology for highly active HER catalysis. Due to the higher electronegativity of P than Ni, it can simultaneously react with Ni at elevated temperatures to form Ni phosphides, creating a unique interface between Ni_2P and $NiTe_2$. Importantly, the generated PH_3 vapor can directly interact with NiTe, inducing a phase transformation from less active NiTe to active $Ni_2P/NiTe_2$ catalyst for alkaline HER. In addition, it is known that metal phosphide/dichalcogenide-based catalysts perform well for HER activity in acidic condition[7, 21]. However, the prepared $Ni_2P/NiTe_2$ electrode is unstable in acid, because the nickel foam substrate which served as the Ni source can react with H_2SO_4 to generate H_2 even without applying a cathodic potential (Fig. S1, ESI†). Thus, we

[a] School of Chemistry, The University of New South Wales, Sydney, NSW 2052, Australia. E-mail: chuan.zhao@unsw.edu.au
[b] School of Physics and Engineering, The Australian National University, Canberra, ACT 2601, Australia.
[c] National Synchrotron Radiation Laboratory, University of Science and Technology of China, Hefei 230029, P. R. China.
†Electronic Supplementary Information (ESI) available: See DOI: 10.1039/x0xx00000x

only measured the HER activity of the $Ni_2P/NiTe_2$ electrode in alkaline in this work.

2 Experimental

2.1 Material synthesis

Synthesis of NiTe nanosheet: The NiTe nanosheet was in situ anchored on nickel foam (NF) through a facile hydrothermal process by using a piece of NF as both the substrate and the Ni source, 0.25 mmol Na_2TeO_3 as Te source and 0.25 mL hydrazine hydrate as the reducing agent, which then dissolved in 10 mL deionized water and put into a Teflon-lined autoclave of 20 mL capacity. After stirring for 10 min, the autoclave was heated at 180 °C for 12 h. After that, the system was allowed to cool to room temperature naturally and the electrode was collected, washed with deionized water and absolute ethanol, and then air-dried at room temperature.

Synthesis of $Ni_2P/NiTe_2$ nanosheet: Briefly, the NiTe electrode on NF was placed in a crucible boat and inserted in the center of a tube furnace equipped with gas controllers. A crucible boat containing different amount of NaH_2PO_2 (0-18 mmol) and NiTe/NF was placed in the upstream and downstream positions in the tube furnace, respectively. Subsequently, the samples were calcinated at 350 °C for 2 h with a heating speed of 3 °C min^{-1} under a flowing Ar atmosphere.

Synthesis of P-NiTe nanosheet: The synthesis procedure of P-NiTe was the same as $Ni_2P/NiTe_2$, except replacing NaH_2PO_2 by red phosphorus powder as the phosphorus precursor.

Synthesis of Ni_2P/NiS_2 electrode: Firstly, Ni_3S_2 was prepared by hydrothermal method, which was in situ grown on NF by using a piece of NF as both the substrate and the Ni source, 0.25 mmol C_2H_5NS as S source and then dissolved in 10 mL deionized water and put into a Teflon-lined autoclave of 20 mL capacity for reaction at 180 °C for 12 h. Then, the same procedure was carried out to prepare the Ni_2P/NiS_2 electrode by using 12 mmol NaH_2PO_2 to generate the PH_3 vapor.

2.2 Physical characterization

Scanning electron microscope (SEM, JSM-7001F) and X-ray diffraction (XRD, Empyrean PANalytical diffractometer, CuKα radiation) were employed for characterizing the prepared sample. Transmission electron microscopy (TEM), high-resolution transmission electron microscopy (HRTEM), and energy-dispersive X-ray spectroscopy (EDS) mapping images were obtained from JEOL F200. Chemical compositions of the samples were analyzed by X-ray photoelectron spectroscopy (XPS, Thermo ESCALAB250i). Atomic force microscopy (AFM) was carried out on a Dimension ICON SPM scanning probe microscope (Bruker AXS S.A.S.).

2.3 Electrochemical measurement

All electrochemical measurements were carried out with a CHI 660 electrochemical workstation. As-prepared $Ni_2P/NiTe_2$ catalyst on NF was directly used as the working electrode without further treatments. A graphite carbon plate and saturated calomel electrode (SCE) with double junction were used as counter electrode and reference electrode, respectively. All potentials measured were calibrated to reversible hydrogen electrode (RHE) using the following equation: $E_{RHE} = E_{SCE} + 0.241\ V + 0.059\ pH$. In our work, we regularly calibrated the used SCE against a master SCE electrode which is kept in saturated KCl solution. The difference between the working SCE electrodes and the master SCE (0.241 V vs RHE) is always kept within ± 3 mV. If the working SCE exhibits shift above ± 3 mV, the reference electrode was reconditioned to achieve ± 3 mV shift. The pH range of the 1 M KOH electrolyte used in this study was measured to 13.70 ± 0.02 by using a Mettler Toledo pH meter. The pH value 13.70 is used in this work for the calibration to reversible hydrogen electrode (RHE). HER linear sweep voltammetry (LSV) polarization curves were recorded at a scan rate of 5 mV s^{-1}. All the HER polarization curves were measured in 1 M KOH with 95% *i*R compensation. Chronoampermetric measurement was obtained under the same experimental setup without *i*R compensation. Electrochemical impedance spectra (EIS) of samples were measured at an overpotential of 200 mV in the frequency range of 0.1-100,000 Hz with amplitude of 10 mV in 1 M KOH electrolyte.

Calculation of electrochemically active surface area (ECSA): The calculation of ECSA is based on the measured double layer capacitance (C_{DL}) of the synthesized electrodes in 1 M KOH. Briefly, a potential range where no apparent Faradaic process happened was determined firstly using the static CVs. The charging current i_c which equals to the product of the scan rate (υ), and the electrochemical double-layer capacitance, C_{DL}, was measured from the CVs at different scan rates and follows the equation:

$$i_c = \upsilon\, C_{DL}$$

Thus, the ECSA is positively correlated with the derived curve slope from the equation.

2.4 Faradaic efficiency

The generated H_2 gases during HER are measured by gas chromatograph (GC). Test conditions: Purge Ar gas (HP 99.99%) for 30 min before electrolysis. TCD for the detection of H_2. In our experiment, we employed a real-time quantitative method to determine the concentration of H_2 and the corresponding Faradaic efficiency (FE). The electrolysis was carried out in a two compartment gastight H-cell at a potential of –1.2 V (*vs*. SCE) for 30 min and the GC detection was carried out and the generated H_2 is detected online by a gas chromatograph system at the electrolysis time of 8 min, 16 min and 24 min, respectively. The FE is calculated to be 99.2 ± 1%, by using the following equation:

$$\mathrm{FE} = \frac{2FV\upsilon p_0}{RT_0 I} \times 100\%$$

$$\mathrm{FE} = \frac{2 \times 96{,}485 \times V\upsilon \times 1.01 \times 10^5}{8.314 \times 298.15 \times I} \times 100\% = \frac{0.315 \times V \times \upsilon}{I} \times 100\%$$

FE = Faradaic efficiency; υ = volume concentration of H_2 in the exhaust gas from the cell; V = Ar flow rate (20 mL min^{-1}).

2.5 DFT calculations

All of the spin-polarized DFT calculations were performed using the VASP program[22-24], which uses a plane-wave basis set and a projector augmented wave method (PAW) for the treatment of core electrons[23]. The generalized gradient approximation of

Perdew, Burke, and Ernzerhof (GGA–PBE)[24] with van der Waals (vdW) correction proposed by Grimme (DFT-D2)[25] was used in all the calculations due to its good description of long-range vdW interactions. For the expansion of wavefunctions over the plane-wave basis set, a converged cutoff was set to 450 eV. Spin-polarization effect and dipole correction were considered in all cases.

To simulate the Ni_2P/NiTe and Ni_2P/$NiTe_2$ interfaces, we place a $Ni_{12}P_6$ cluster on a 3×2×5 NiTe(011) surface and a 4×2×6 $NiTe_2$(011) surface, respectively, with a 20 Å vacuum between the slabs. It should be noted that in our simulations, we used 2×2×4 slabs (not $Ni_{12}P_6$ cluster) with periodical boundary conditions to mimic Ni_2P(111) surface. However, to simulate Ni_2P/NiTe and Ni_2P/$NiTe_2$ interfaces, we added a Ni_2P cluster on NiTe(011) and $NiTe_2$(011) surfaces, which was built based on Ni_2P bulk crystal and resembles the Ni_2P (111) surface structure. The $Ni_{12}P_6$ cluster was built based on Ni_2P bulk crystal and resembles the Ni_2P (111) surface structure. The Brillouin zone was sampled using 3×4×1 Γ-centered mesh. In geometry optimizations, the upper most layer (including the $Ni_{12}P_6$ cluster and the top two atomic layers of NiTe(011) or $NiTe_2$(011) slab) were relaxed while the other layers were fixed at the bulk lattice position. For comparison, a 3×2×5 NiTe(011) slab and a 4×2×6 $NiTe_2$(011) slab was used to simulate the NiTe(011) and $NiTe_2$(011) surfaces, respectively. The Ni_2P (111) surface was modeled by a 2×2×4 slab, and the top two atomic layers were relaxed while the other layers were fixed at the bulk lattice position. The Brillouin zone was sampled using 3 × 3 × 1 Γ-centered mesh. The convergence threshold in all the calculations was set as 10^{-4} eV in energy and 0.005 eV $Å^{-1}$ in force.

The overall hydrogen evolution reaction (HER) mechanism is evaluated with a three-state diagram consisting of an initial H^+ state, an intermediate H^* state, and 1/2 H_2 as the final product. The free energy of H^* (ΔG_{H^*}) is proven to be a key descriptor to characterize the HER activity of the electrocatalyst. A electrocatalyst with a positive value leads to low kinetics of adsorption of hydrogen, while a catalyst with a negative value leads to low kinetics of release of hydrogen molecule[26]. The optimum value of $|\Delta G_{H^*}|$ should be zero; for instance, this value for the well-known highly efficient Pt catalyst is near-zero as $|\Delta G_{H^*}| \approx 0.09$ eV. The ΔG_{H^*} is calculated as：[26]

$$\Delta G_{H^*} = \Delta E_{H^*} + \Delta E_{ZPE} - T\Delta S_H$$

where ΔE_{H^*} is the binding energy of adsorbed hydrogen, and ΔE_{ZPE} and ΔS_H are the difference in ZPE and entropy between the adsorbed hydrogen and hydrogen in the gas phase, respectively. As the contribution from the vibrational entropy of hydrogen in the adsorbed state is negligibly small, the entropy of hydrogen adsorption is $\Delta S_H \approx -0.5 S_{H_2}$, where S_{H_2} is the entropy of H_2 in the gas phase at the standard conditions. Therefore, the ΔG_{H^*} value for various studied catalysts should be $\Delta E_H + 0.24$ eV[6].

3 Results and discussion

The heterostructures of Ni_2P/$NiTe_2$ catalyst was prepared through a two-step process, as illustrated in Fig. 1a. The thin NiTe nanosheet was firstly grown onto nickel foam (NF) through a hydrothermal reaction, where N_2H_4 is used as a reducing and complexing agent to react with Na_2TeO_3 to form NiTe. The formation of NiTe can be visually detected from the color change of NF from silver white to black after reaction (Fig. S2, ESI†). Ni_2P/$NiTe_2$ heterostructures with controlled crystalline phases and thicknesses from 1.5 nm to 7.5 nm can be produced by a high temperature annealing process at different PH_3 vapor concentrations (from 0 mmol to 18 mmol). The Ni_2P/$NiTe_2$ electrode prepared using 12 mmol NaH_2PO_2 was discussed in the following sections, unless otherwise stated, as it shows the highest HER activity.

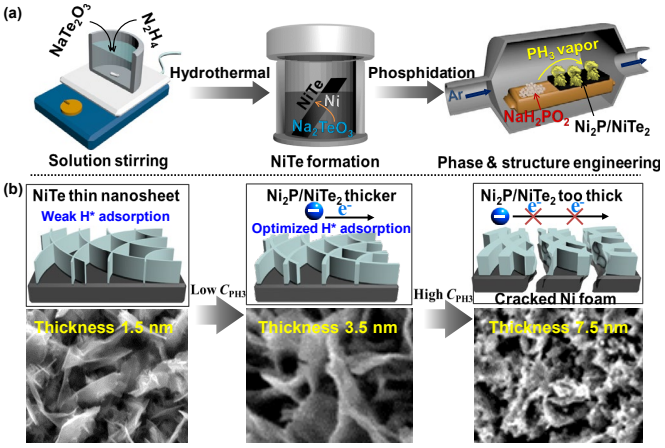

Fig. 1 (a) Schematic illustration of the two-step synthesis of Ni_2P/$NiTe_2$. (b) The fabricated catalysts with different structures and nanosheet thicknesses and the reaction mechanisms for the enhanced HER activity on Ni_2P/$NiTe_2$ with a nanosheet thickness of 3.5 nm. C_{PH3} is the concentration of PH_3 vapor.

The morphology of the catalysts obtained was firstly characterized by scanning electron microscopy (SEM). Hydrothermally grown NiTe/NF shows thin nanosheet morphology (Fig. S3, ESI†). The morphology of the Ni_2P/$NiTe_2$ electrode largely maintains the nanosheet structure of NiTe, but with a slightly increased thickness. The transmission electron microscopy (TEM) of Ni_2P/$NiTe_2$ also demonstrates the well-kept nanosheet morphology (Fig. 2b). The high resolution TEM (HRTEM) in Fig. 2c shows the lattice spacing of 0.28 nm and 0.29 nm, which corresponds to the (011) lattice plane of $NiTe_2$ and NiTe, respectively, and a lattice spacing of 0.22 nm assigned to the (111) facet of Ni_2P. The formation of heterostructures is further confirmed by the selected area electron diffraction (SAED) pattern (Fig. 2d) which shows the diffraction spots of (111) for Ni_2P and (011) for $NiTe_2$ and NiTe. Moreover, TEM energy dispersive X-ray spectroscopy (EDS) mapping also confirms that Ni, Te and P are all uniformly distributed in the nanosheet (Fig. 2e-g). However, P and Te appear mainly localized in the Ni_2P, $NiTe_2$ and NiTe parts of the nanosheet (Fig. 2f-h), further implying the formation of heterostructures and Ni_2P/$NiTe_2$ interfaces

X-ray diffraction analysis (XRD) was used to investigate the crystal structure of the composite. As shown in Fig. 2i, the XRD patterns of NiTe grown on NF shows peaks of (011), (002), (012), (110) and (021) at 30.9°, 33.4°, 42.8°, 45.7° and 56.2°, respectively (ICDD No. 98-004-2557, or JCPDS No. 38-1393), which matched with the hexagonal NiTe phase. It should be noted that in some literatures[27-29], the main peak at 30.9° is assigned to (101) plane of NiTe. However, in hexagonal structure of the same material, (101) and (011) are crystallographically equivalent (see Fig. S4, ESI†), because they are in the same family of planes of NiTe, by extension, {011} family. The peaks at 44.4° and 51.7° arise from the underlying NF substrate. Apart from the main peaks for NiTe, the peaks at

27.6° and 29.8° are attributed to TeO_2 formed during hydrothermal reactions by the reaction between Te and H_2O. For comparison, pure Ni_2P was also prepared which shows characteristic peaks at 40.5°, 47.2°, 48.8° and 54.1° for (111), (210), (002) and (300) facets of hexagonal Ni_2P (ICDD: 00-003-0953). For the $Ni_2P/NiTe_2$ electrode, the diffraction peaks for NiTe and Ni_2P can be indexed. However, a new peak emerges at 31.7° attributed to (011) plane of $NiTe_2$ (ICDD No. 04-003-1928 or JCPDS No. 89-2642). At the same time, the peaks at 29.8° for TeO_2 decrease to some extent, which demonstrates that the PH_3 vapor not only can reduce TeO_2, but also induce the formation of Ni_2P and trigger the phase transformation from NiTe to $NiTe_2$. Two control samples were prepared to further demonstrate the important role of PH_3 vapor. One control sample was fabricated by annealing NiTe in Ar without NaH_2PO_2, and the other was prepared by annealing NiTe using red phosphorus as the P source. For both samples, the XRD spectra showed almost identical XRD patterns with NiTe (Fig. S5 and S6, ESI†), highlighting the PH_3 vapor is key to the phase transformation and heterostructures formation.

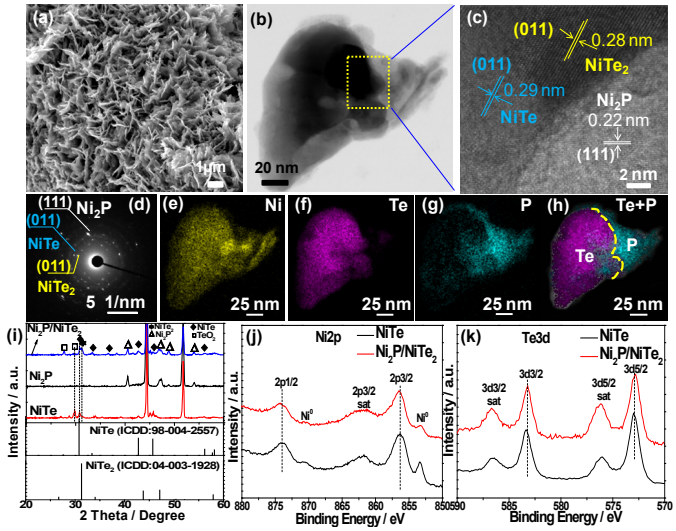

Fig. 2 (a) SEM, (b) TEM, (c) HRTEM, (d) SAED and (e-g) the corresponding elemental mapping images for Ni, Te, P elements and (h) the overlapping of Te and P elements in $Ni_2P/NiTe_2$. (i) XRD patterns of NiTe, Ni_2P and $Ni_2P/NiTe_2$. High-resolution XPS spectra of (j) Ni2p and (k) Te3d of NiTe and $Ni_2P/NiTe_2$.

The surface chemical composition and oxidation state of the prepared NiTe and $Ni_2P/NiTe_2$ catalysts were analyzed by X-ray photoelectron spectroscope (XPS). For NiTe, the high-resolution Ni2p (Fig. 2j) shows peaks at around 856.3 and 874.0 eV that can be assigned to Ni^{2+} 2p3/2 and Ni^{2+} 2p1/2 of NiTe, respectively. The peaks at about 853.2 eV and 871.7 eV belong to Ni^0 derived from NF substrate. For Te3d, the peaks at 572.9 eV and 583.3 eV correspond to Te^{2-} 3d 5/2 and Te^{2-} 3d 3/2 of NiTe and the other satellite peaks result from the oxidation of Te on the surface[30]. Similar XPS spectra are obtained for the $Ni_2P/NiTe_2$ electrode. The P2p core-level XPS shows two peaks centered at 129.7 eV and 134.0 eV (Fig. S7, ESI†), which match with the energy of Ni-P bond and phosphate groups, respectively. When comparing the Ni2p and Te3d spectra of $Ni_2P/NiTe_2$ with NiTe, almost no peaks shift were observed for all the prepared samples including the different amount of NaH_2PO_2 treated samples (Fig. 2j, k and Fig. S8, ESI†), which indicates the electronic interaction between Ni_2P and $NiTe_2$ are not the reason for the enhanced HER activity. This unobvious electronic interaction between Ni_2P and $NiTe_2$ also has been confirmed from DFT calculations (see below). However, the XPS peaks data ratios for metal phosphide/phosphate are 8.9%, 12.3% and 16.2%, respectively, with the increment of the amount of NaH_2PO_2 from 6 mmol to 18 mmol, indicating a higher degree of metal phosphide was formed at high NaH_2PO_2 concentration.

The catalytic activities of $Ni_2P/NiTe_2$ and the control samples were studied for HER in 1 M KOH electrolyte. To optimize the HER performance, a set of $Ni_2P/NiTe_2$ electrodes were prepared by adjusting the amount of NaH_2PO_2 used in the annealing process for generating different concentrations of PH_3 vapor. As shown in Fig. S9 (ESI†), pure NiTe shows almost same HER performance as NF substrate, indicating it is less active to HER. The best HER performance was obtained for the $Ni_2P/NiTe_2$ electrode fabricated by using 12 mmol NaH_2PO_2 to generate the PH_3 vapor (Fig. S10, ESI†). The deficiency or excess of NaH_2PO_2 results in lower HER performance and the reason was studied. Fig. S11 (ESI†) shows the XRD spectra of the samples obtained with various amount of NaH_2PO_2. It is found that the thermal annealing at different PH_3 vapor concentrations is effective to regulate both the crystalline phase and morphology of the catalysts. At low PH_3 concentration (6 mmol NaH_2PO_2), there is no obvious peak for $NiTe_2$. In this case, Ni_2P/NiTe was fabricated and relatively small enhanced HER activity was observed (Fig. S10, ESI†). As the electrochemical activity and theoretical results (see below) both demonstrate that the $Ni_2P/NiTe_2$ heterostructures are more active and contribute more to the observed HER activity, thus, the $Ni_2P/NiTe_2$ is named for our catalyst so as to highlight the key role of the $Ni_2P/NiTe_2$ interface on the enhanced activity. With the increment of the PH_3 vapor (12 mmol and 18 mmol NaH_2PO_2), the characteristic peaks at 30.9° for NiTe gradually weakened and finally disappeared, while the 31.7° peak for $NiTe_2$ gets stronger and becomes dominant, indicating high PH_3 vapor concentration favors for the formation of $NiTe_2$. However, the sample annealed at high PH_3 vapor concentrations on NF is fragile, which can be viewed from the apparently damaged NF with an abundance of cracked features (Fig. S12a, ESI†). In addition, thick and densely distributed nanosheets were obtained (Fig. S12b, c, ESI†), which can be identified by atomic force microscopy (AFM). For NiTe without PH_3, the AFM image clearly showed thin nanosheets with an average thickness of ~1.5 nm (Fig. S13, ESI†). With the increase of PH_3, the nanosheet thickness increased to ~3.5 nm and ~7.5 nm for the samples prepared with 12 mmol (Fig. S14, ESI†) and 18 mmol (Fig. S15, ESI†) NaH_2PO_2, respectively. The collapsed NF substrate and the thick nanosheet are unfavorable for electron transfer and have less exposed active sites, thus show decreased HER performance, as illustrated in Fig. 1b.

The catalytic performance of $Ni_2P/NiTe_2$ electrode prepared with 12 mmol NaH_2PO_2 was further investigated, together with the control samples of NiTe, Ni_2P and commercial Pt/C (20 wt% Pt on carbon black). As shown in Fig. 3a, the $Ni_2P/NiTe_2$ electrode delivers significantly higher current density and lower overpotential than bare NiTe and Ni_2P for HER, suggesting the constructed $Ni_2P/NiTe_2$ interfaces are keys to the enhanced HER performance. For example, the $Ni_2P/NiTe_2$ shows a small overpotential of 62 mV to achieve a current density of -10 mA cm^{-2}, much lower than that of 195 mV for NiTe and 107 mV for Ni_2P. Moreover, to deliver a current density of -100 mA cm^{-2}, it only requires an overpotential of 143 mV, whereas 294 mV and 199 mV are needed for NiTe and Ni_2P electrodes, respectively. Although these values are larger than the 18 mV (@-

10 mA cm^{-2}) and 42 mV (@-100 mA cm^{-2}) overpotential required on Pt/C, these results are comparable or better than that of recently reported noble-metal-free HER catalysts with/without heterostructures with comparable mass loading ($Ni_2P/NiTe_2$ catalyst mass loading on NF is: 1.4 ± 0.2 mg cm^{-2}, Table S1, ESI†)[13, 14, 31-33].

To gain insights into the reaction kinetic mechanism of the prepared electrodes, Tafel slopes were obtained for the prepared samples. As shown in Fig. 3b, the Tafel slope for $Ni_2P/NiTe_2$ is 80 mV dec^{-1}, which is smaller than that of NiTe (111 mV dec^{-1}) and Ni_2P (86 mV dec^{-1}), suggesting that the HER at $Ni_2P/NiTe_2$ follows a Volmer-Heyrovsky mechanism[34]. For Pt/C, a Tafel slope of 29 mV dec^{-1} was obtained. The exchange current density (j_0) values of the electrodes were also calculated through the extrapolation of Tafel plots (Fig. S16, ESI†). The j_0 value of 2.41 mA cm^{-2} is obtained for $Ni_2P/NiTe_2$, which is 4 and 15 times larger than that of 0.61 and 0.16 mA cm^{-2} for Ni_2P and NiTe, respectively. This demonstrates the $Ni_2P/NiTe_2$ interfaces can boost the electron transfer rates and the intrinsic catalytic activities of the catalyst for HER.

The long-term stability of the electrocatalyst is further evaluated for practical applications. As shown in Fig. 3c, the potential of the $Ni_2P/NiTe_2$ electrode remains stable for over 20 h and even 50 h (Fig. S17, ESI†) of HER at a constant current density of -50 mA cm^{-2}. The LSV curves recorded before and after the long-term stability test almost overlay with each other (Fig. 3d), evidencing excellent long-term stability. The structure and morphology of the $Ni_2P/NiTe_2$ electrode was studied by the post-electrolysis characterizations of the catalyst via XRD, TEM-EDS mapping and XPS. The XRD spectra of the electrode after HER shows an unchanged XRD pattern (Fig. S18, ESI†), while the TEM-EDS mapping shows the co-existence of Ni, Te and P (Fig. S19, ESI†). Moreover, the XPS spectra after HER also show the signals for Ni, Te and P, with the characteristic nickel phosphide peak at 129.7 eV (Fig. S20, ESI†). The atomic ratios of the elements after normalization to Ni are $NiTe_{0.28}P_{0.71}$ and $NiTe_{0.27}P_{0.67}$ before and after HER by analyzing the XPS results, indicating there is a slight dissolution of Te and P after HER. In addition, the atomic ratios of the elements were further studied by inductively coupled plasma optical emission spectroscopy (ICP-OES). The elemental ratios after normalization to Ni are $NiTe_{0.32}P_{0.70}$ and $NiTe_{0.30}P_{0.65}$, before and after HER. These results are close to the results tested by XPS. The dissolution was likely due to the corrosion of the catalyst by KOH, which resulted in slightly decreased catalytic activity after stability, as shown in Fig. 3d.

In addition, we have compared the $Ni_2P/NiTe_2$ XPS before and after HER. As shown in Fig. S20 (ESI†), the Ni^0 peaks at around 852.8 eV and 871.7 eV are attributes to the underneath NF substrate. The existence of Ni2p3/2 and Ni2p1/2 peaks can be assigned to Ni^{2+} oxidation state in the $Ni_2P/NiTe_2$ composite. By comparing the XPS spectra before and after stability, we have not observed clear shift of binding energies at Ni2p. However, a positive binding energy shift were observed at the Te3d and P2p XPS spectra after HER, which can be attributed to the oxidation when the sample was exposed to air or the oxidation of the element by the dissolved oxygen in the electrolyte. For the valence state of Te, the peaks at Te3d5/2 and Te3d3/2 correspond to Te^{2-} in the $Ni_2P/NiTe_2$ catalyst, while their corresponding satellite peaks result from the oxidation of Te on the surface. For P2p, both metal phosphide and phosphate were observed before and after HER. However, different from the slightly positive shifted metal phosphate peak, the metal phosphide peak shows less change, demonstrating the formed Ni_2P is stable during long-term water electrolysis.

Moreover, the estimated weight percentage of Ni in the $Ni_2P/NiTe_2$ compound is ~50%, which is between that of 78.9% in Ni_2P and 18.5% in $NiTe_2$. In comparison to the literatures, this weight percentage is close to the average of the reported values. For example, the HER overpotential appears to be lower in the case of electrodeposited Ni-Co alloys with a weight percentage ranging between 35% and 64% in alkaline media[35,36]. Other reports indicate that the weight percentage of Ni accounts for 80% of the electrodeposited Ni/P catalyst shows the best HER activity[37]. Furthermore, the generated H_2 gas was qualified by gas chromatography (GC) and a Faradaic efficiency of 99.2 ± 1 % is obtained (see more details in Fig. S21, ESI†).

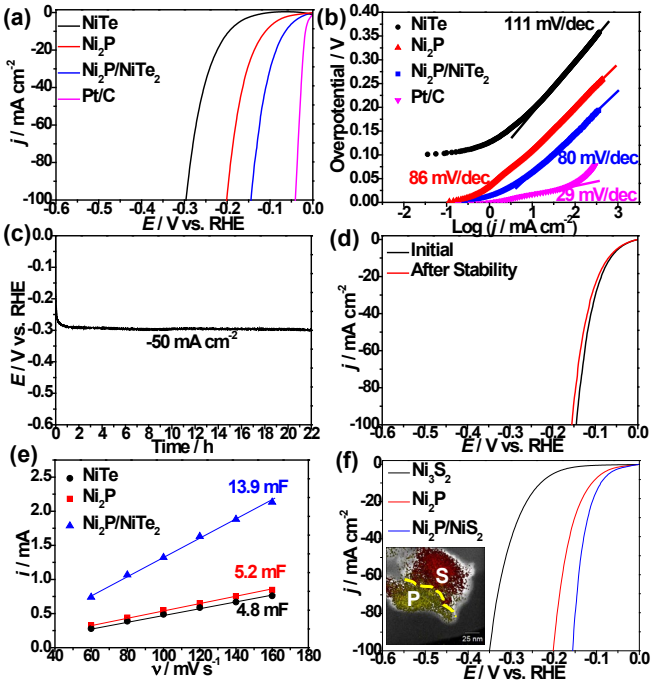

Fig. 3 (a) The HER polarization curves and (b) the corresponding Tafel plots of NiTe, Ni_2P, $Ni_2P/NiTe_2$ and commercial Pt/C. (c) Time-dependent potential curves of the $Ni_2P/NiTe_2$ electrode under a static current density of -50 mA cm^{-2} without *iR* correction and (d) the polarization curves comparison before and after stability. (e) Extraction of the C_{dl} from different electrodes and (f) polarization curves of Ni_2P/NiS_2 electrode and the control samples.

In order to understand the origin of the HER performance of $Ni_2P/NiTe_2$, the double-layer capacitance (C_{dl}) of the electrode was measured in the non-Faraday region to estimate the electrochemical surface area (ECSA) (Fig. S22, ESI† and Fig. 3e). As expected, the $Ni_2P/NiTe_2$ electrode exhibits the largest C_{dl} of 13.9 mF, which is 2.9 and 2.7 times higher than that of NiTe (4.8 mF) and Ni_2P (5.2 mF), indicating the heterostructures provide more active surface area for HER. In addition, to understand the intrinsic HER activities of each active site, the specific activity with current normalized against ECSA was analyzed. Fig. S23 (ESI†) shows that after considering the surface area effect, the $Ni_2P/NiTe_2$ electrode still shows higher HER activity than NiTe and Ni_2P, revealing the $Ni_2P/NiTe_2$ interface is of great importance to the accelerated HER kinetics.

Furthermore, the HER reaction kinetics and charge transfer process of the samples were studied by electrochemical impedance

spectroscopy (EIS). Fig. S24 (ESI†) shows typical Nyquist plots of the $Ni_2P/NiTe_2$, NiTe, and Ni_2P electrodes. An equivalent resistor-capacitor circuit model was used to fit the impedance spectra, as shown in the inset of Fig. S24 (ESI†), which consists of a resistor (R_s), representing the resistance of the electrolyte solution; a charge transfer resistance (R_{ct}), representing the charge transfer resistivity; and a capacitance (C) in parallel with R_{ct}, analogous to the double layer charging capacity of the solid-liquid junction. The EIS spectra reveal a smaller charge transfer resistance for the $Ni_2P/NiTe_2$ electrode (5.3 Ω) than that of NiTe (19.2 Ω) and Ni_2P (7.9 Ω), suggesting faster electron transfer kinetics of HER at $Ni_2P/NiTe_2$ electrode.

To understand the effects of $Ni_2P/NiTe_2$ interfaces on HER, a series of density functional theory (DFT) calculations were carried out for $Ni_2P/NiTe_2$ and $Ni_2P/NiTe$ heterostructures, and compared with Ni_2P, $NiTe_2$ and NiTe. All the theoretical model structures are shown in Fig. S25 (ESI†). Here, we considered the key reaction steps in alkaline HER, including the water dissociation reaction and the adsorption/combination of reaction hydrogen intermediates (H*)[38]. For alkaline HER, water supplies hydrogen and the water dissociation reaction is considered as a key rate determining step[38, 39]. Fig. S26 (ESI†) shows the calculated reaction energy diagram of water dissociation on $NiTe_2$(011), NiTe(011), $Ni_2P/NiTe_2$(011) and $Ni_2P/NiTe$(011). The energy barriers for water dissociation are 1.85 eV and 1.78 eV on NiTe(011) and $NiTe_2$(011), respectively, and such high energy barriers clearly hinders the dissociation of water on NiTe(011) and $NiTe_2$(011). However, the water dissociation barrier is reduced to 1.45 eV on $Ni_2P/NiTe_2$(011) surface, which indicate $Ni_2P/NiTe_2$(011) surface can promote water dissociation substantially and increase the rate of H* formation.

Fig. 4c shows the calculated free energy diagram for HER on Ni_2P(111), $NiTe_2$(011), NiTe(011), $Ni_2P/NiTe_2$(011) and $Ni_2P/NiTe$(011) with the most energetically stable configurations, and the corresponding optimized structures of H* adsorbed on these catalysts are shown in Fig. 4a, b and Fig. S27 (ESI†). For the $NiTe_2$(011) and NiTe(011), the free energies of H* (ΔG_{H^*}) are quite positive (0.53~0.54 eV), which indicates a weak interaction between H* and catalyst surfaces, manifesting in poor HER reaction kinetics. In contrast, the ΔG_{H^*} is -0.21 eV for Ni_2P(111), suggesting a slightly stronger binding of H* on Ni_2P(111) relative to ideal HER catalyst (the optimum value of $|\Delta G_{H^*}|$ should be zero[26]). Importantly, it is found that the $Ni_2P/NiTe_2$ and $Ni_2P/NiTe$ interfaces have significant effects on HER. The H* adsorbed at the interfaces of $Ni_2P/NiTe_2$(011) and $Ni_2P/NiTe$(011) can simultaneously bind to two Ni atoms (a Ni of Ni_2P cluster and another Ni of $NiTe_2$(011) or NiTe(011) surface, as shown in Fig. 4a and b), which greatly enhanced the H* binding on $Ni_2P/NiTe_2$(011) and $Ni_2P/NiTe$(011) compared to $NiTe_2$(011) and NiTe(011). Especially, the value of ΔG_{H^*} on $Ni_2P/NiTe_2$(011) is reduced to 0.01 eV, which is close to ideal HER catalyst and much smaller than other control samples, indicating the superior HER activities compared to $Ni_2P/NiTe$ (011), Ni_2P(111), $NiTe_2$(011), and NiTe(011). Of note, to further elucidate the NiTe (011) plane is the same as NiTe (101) plane that widely used in the literatures, we have calculated the free energy of H* (ΔG_{H^*}) at NiTe(101) and $Ni_2P/NiTe$(101). The calculation results show that they have the same value of 0.54 eV and 0.16 eV, respectively (Fig. S28, ESI†), as that calculated on NiTe(011) and $Ni_2P/NiTe$(011), because they are in the same family of planes of NiTe, that is the {011} family. Moreover, to gain the interface effects on H* binding on $Ni_2P/NiTe_2$(011) during HER, we analyzed the amount of electrons transferred from Ni atoms to H* on $Ni_2P/NiTe_2$(011) and $NiTe_2$(011) based on the Bader analysis[40]. We found that more electrons transfer from Ni atoms to H* on $Ni_2P/NiTe_2$(011) (0.22 e^-) compared to that on $NiTe_2$(011) (0.13 e^-), which can explain the enhanced H* binding on $Ni_2P/NiTe_2$(011). The HER activities of various catalysts follows the order in the sequence of $Ni_2P/NiTe_2$(011) > $Ni_2P/NiTe$(011) > Ni_2P > $NiTe_2$(011) > NiTe(011), which are in good agreement with the experimental observations that the formed $Ni_2P/NiTe_2$ interfaces are the real active sites of the enhanced HER activities. It should be noted that we also investigated the electron interaction between Ni_2P and $NiTe_2$ by calculating the charge state on Ni at the heterostructures interface. As seen from Table S2 (ESI†), the Ni charge states at the Ni_2P(111)/NiTe(011) or Ni_2P(111)/$NiTe_2$(011) interface show little change compared to NiTe(011) or $NiTe_2$(011) after introducing Ni_2P into the heterostructures, which is consistent with the XPS results. This indicates that compared to the electronic interaction effect, the $Ni_2P/NiTe_2$(011) interfaces play a more important role for the enhanced HER activity, as we discussed above.

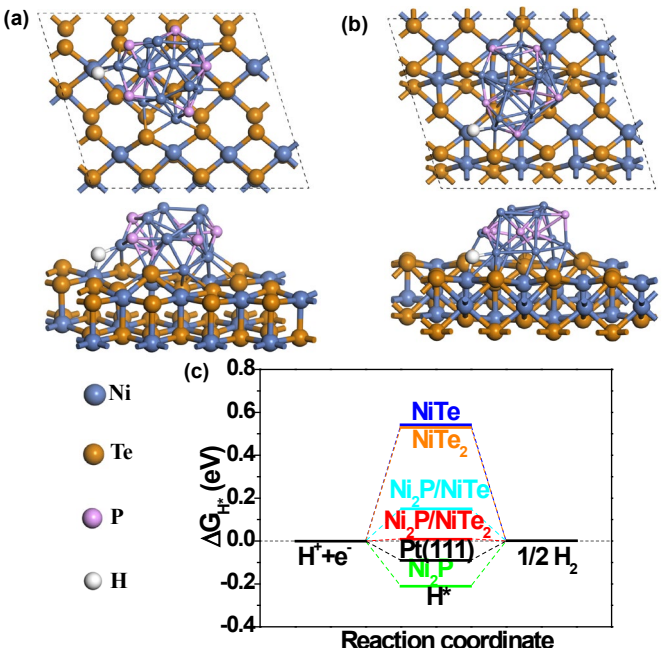

Fig. 4 The top (up) and side (down) views of the optimized structures of H* adsorbed on (a) $Ni_2P/NiTe_2$(011) and (b) $Ni_2P/NiTe$(011). The steel blue, dark orange, magenta and white balls represent Ni, Te, P and H atoms, respectively. (c) The calculated ΔG_{H^*} diagram of the HER at the equilibrium potential for various catalysts. The values for Pt(111) is also shown here for comparison.

Finally, we demonstrate this phase transformation strategy can be extended to other metal-dichalcogenides to prepare active heterostructured catalysts for HER. In this case, a Ni_3S_2 electrode grown on NF was prepared by a hydrothermal reaction and then annealed in a PH_3 vapor environment. Following the PH_3 treatment, new phases of Ni_2P, Ni_3P and NiS_2 appeared, evidenced from the XRD pattern (Fig. S29, ESI†). The formation of the heterostructures is evidenced from the TEM-EDS elemental mapping, where a clear

Ni_2P/NiS_2 interface was observed (Fig. S30, ESI†). As shown in Fig. 3f, the obtained Ni_2P/NiS_2 electrode shows a significantly enhanced HER activity with an overpotential of 87 mV to reach -10 mA cm^{-2} and 156 mV to reach -100 mA cm^{-2}, better than the activity of Ni_2P and Ni_3S_2. Furthermore, the ECSA measurements indicate that Ni_2P/NiS_2 heterostructures offer large active surface area (Fig. S31, S32, ESI†), which improves the electrocatalytic performance of the electrode. After considering the surface area effect, the Ni_2P/NiS_2 electrode still shows higher HER activity than Ni_3S_2 and Ni_2P (Fig. S33, ESI†), indicating the Ni_2P/NiS_2 interface is of great importance to the accelerated HER kinetics.

4 Conclusions

In summary, a facile PH_3 vapor treatment approach was developed to fabricate heterostructured $Ni_2P/NiTe_2$ catalysts with a controlled crystalline phase and morphology for efficient HER. The phase transformations as well as the morphological engineering have experimentally and theoretically proved to be an effective way to enhance alkaline HER electrolysis. Importantly, it is also applicable to treat less active chalcogenide-based materials, such as Ni_3S_2, for production of active Ni_2P/NiS_2 interfaces with enhanced HER catalysis, by treating the Ni_3S_2 electrode with PH_3 vapor. The present study highlights a general synthetic approach by using PH_3 vapor for phase and structural engineering to create high-performance electrocatalysts for HER and important electrochemical reactions beyond.

Conflicts of interest

There are no conflicts to declare.

Acknowledgements

Y. Li and X. Tan contributed equally to this work. All physical characterizations were carried out at the Mark Wainwright Analytical Centre (MWAC) at the University of New South Wales (UNSW). We give special thanks to Dr. Yin Yao from MWAC for his help to collect the AFM images, Dr. Bin Gong for XPS and Mr. Tim Fang for his proof-reading of this manuscript. C. Zhao acknowledges the award of Future Fellowship from Australian Research Council (FT170100224).

References

1. N. S. Lewis and D. G. Nocera, *Proc. Natl. Acad. Sci.*, 2006, **103**, 15729-15735.
2. Y. H. Li, P. F. Liu, L. F. Pan, H. F. Wang, Z. Z. Yang, L. R. Zheng, P. Hu, H. J. Zhao, L. Gu and H. G. Yang, *Nat .Commun.*, 2015, **6**, 8064.
3. A. B. Laursen, K. R. Patraju, M. J. Whitaker, M. Retuerto, T. Sarkar, N. Yao, K. V. Ramanujachary, M. Greenblatt and G. C. Dismukes, *Energ. Environ. Sci.*, 2015, **8**, 1027-1034.
4. C. G. Morales-Guio, L. A. Stern and X. L. Hu, *Chem. Soc. Rev.*, 2014, **43**, 6555-6569.
5. H. J. Yin, S. L. Zhao, K. Zhao, A. Muqsit, H. J. Tang, L. Chang, H. J. Zhao, Y. Gao and Z. Y. Tang, *Nat. Commun.*, 2015, **6**, 6430.
6. K. Jiang, B. Y. Liu, M. Luo, S. C. Ning, M. Peng, Y. Zhao, Y. R. Lu, T. S. Chan, F. M. F. de Groot and Y. W. Tan, *Nat. Commun.*, 2019, **10**, 1743.
7. S. Chandrasekaran, L. Yao, L. B. Deng, C. Bowen, Y. Zhang, S. M. Chen, Z. Q. Lin, F. Peng and P. X. Zhang, *Chem. Soc. Rev.*, 2019, **48**, 4178-4280.
8. Y. Hou, M. R. Lohe, J. Zhang, S. H. Liu, X. D. Zhuang and X. L. Feng, *Energ. Environ. Sci.*, 2016, **9**, 478-483.
9. W. F. Chen, K. Sasaki, C. Ma, A. I. Frenkel, N. Marinkovic, J. T. Muckerman, Y. M. Zhu and R. R. Adzic, *Angew. Chem. Int. Edit.*, 2012, **51**, 6131-6135.
10. G. Q. Zhao, K. Rui, S. X. Dou and W. P. Sun, *Adv. Funct. Mater.*, 2018, **28**, 1803291.
11. D. D. Zhu, J. L. Liu, Y. Q. Zhao, Y. Zheng and S. Z. Qiao, *Small*, 2019, **15**, 1805511.
12. Z. J. Zhu, H. J. Yin, C. T. He, M. Al-Mamun, P. R. Liu, L. X. Jiang, Y. Zhao, Y. Wang, H. G. Yang, Z. Y. Tang, D. Wang, X. M. Chen and H. J. Zhao, *Adv. Mater.*, 2018, **30**, 1801171.
13. B. Wang, Z. G. Wang, X. Q. Wang, B. J. Zheng, W. L. Zhang and Y. F. Chen, *J. Mater. Chem. A*, 2018, **6**, 12701-12707.
14. X. L. Zhou, Y. Liu, H. X. Ju, B. C. Pan, J. F. Zhu, T. Ding, C. D. Wang and Q. Yang, *Chem. Mater.*, 2016, **28**, 1838-1846.
15. H. Liu, X. Ma, Y. Rao, Y. Liu, J. L. Liu, L. Y. Wang and M. B. Wu, *ACS Appl. Mater. Interfaces*, 2018, **10**, 10890-10897.
16. U. De Silva, J. Masud, N. Zhang, Y. Hong, W. P. R. Liyanage, M. A. Zaeem and M. Nath, *J. Mater. Chem. A*, 2018, **6**, 7608-7622.
17. C. Wan, Y. N. Regmi and B. M. Leonard, *Angew. Chem. Int. Edit.*, 2014, **53**, 6407-6410.
18. H. Q. Zhou, F. Yu, Y. Y. Liu, J. Y. Sun, Z. A. Zhu, R. He, J. M. Bao, W. A. Goddard, S. Chen and Z. F. Ren, *Energ. Environ. Sci.*, 2017, **10**, 1487-1492.
19. Y. Y. Zhong, B. Chang, Y. L. Shao, C. W. Xu, Y. Z. Wu and X. P. Hao, *ChemSusChem*, 2019, **12**, 2008-2014.
20. S. Wang, D. Zhang, B. Li, C. Zhang, Z. G. Du, H. M. Yin, X. F. Bi and S. B. Yang, *Adv. Energy Mater.*, 2018, **8**, 1801345.
21. J. Y. Sun, M. Q. Ren, L. Yu, Z. Yang, L. X. Xie, F. Tian, Y. Yu, Z. F. Ren, S. Chen and H. Q. Zhou, *Small*, 2019, **15**, 1804272.
22. G. Kresse and J. Hafner, *Phys. Rev. B*, 1994, **49**, 14251-14269.
23. G. Kresse and D. Joubert, *Phys. Rev. B*, 1999, **59**, 1758-1775.
24. G. Kresse and J. Furthmuller, *Phys. Rev. B*, 1996, **54**, 11169-11186.
25. S. Grimme, *J. Comput. Chem.*, 2006, **27**, 1787-1799.
26. J. K. Norskov, T. Bligaard, A. Logadottir, J. R. Kitchin, J. G. Chen, S. Pandelov and J. K. Norskov, *J. Electrochem. Soc.*, 2005, **152**, J23-J26.
27. Z. Q. Xue, X. Li, Q. L. Liu, M. K. Cai, K. Liu, M. Liu, Z. F. Ke, X. L. Liu and G. Q. Li, *Adv. Mater.*, 2019, **31**, 1900430.
28. Z. J. Wang, P. Guo, M. Liu, C. Guo, H. J. Liu, S. X. Wei, J. Zhang and X. Q. Lu, *ACS Appl. Energ. Mater.*, 2019, **2**, 3363-3372.
29. K. S. Bhat, H. C. Barshilia and H. S. Nagaraja, *Int. J. Hydrogen Energy*, 2017, **42**, 24645-24655.
30. D. Yao, Y. Liu, W. J. Zhao, H. T. Wei, X. T. Luo, Z. N. Wu, C. W. Dong, H. Zhang and B. Yang, *Nanoscale*, 2013, **5**, 9593-9597.
31. R. Boppella, J. Tan, W. Yang and J. Moon, *Adv. Funct. Mater.*, 2019, **29**, 1807976.
32. M. Gong, W. Zhou, M. C. Tsai, J. G. Zhou, M. Y. Guan, M. C. Lin, B. Zhang, Y. F. Hu, D. Y. Wang, J. Yang, S. J. Pennycook, B. J. Hwang and H. J. Dai, *Nat. Commun.*, 2014, **5**, 4695.
33. L. Najafi, S. Bellani, R. Oropesa-Nunez, A. Ansaldo, M. Prato, A. E. D. Castillo and F. Bonaccorso, *Adv. Energy Mater.*, 2018, **8**, 703212.
34. R. Miao, B. Dutta, S. Sahoo, J. K. He, W. Zhong, S. A. Cetegen, T. Jiang, S. P. Alpay and S. L. Suib, *J. Am. Chem. Soc*, 2017, **139**, 13604-13607.
35. C. Lupi, A. Dell'Era and M. Pasquali, *Int. J. Hydrogen Energ*, 2009, **34**, 2101-2106.
36. I. Herraiz-Cardona, E. Ortega, J. G. Anton and V. Perez-Herranz, *Int. J. Hydrogen Energ*, 2011, **36**, 9428-9438.
37. J. Li, Y. Zhao, A. L. Wu and Y. X. Wang, *Int. J. Electrochem. Sc*, 2019, **14**, 7582-7593.
38. P. T. Wang, X. Zhang, J. Zhang, S. Wan, S. J. Guo, G. Lu, J. L. Yao and X. Q. Huang, *Nat. Commun.*, 2017, **8**, 14580.
39. R. Subbaraman, D. Tripkovic, D. Strmcnik, K. C. Chang, M. Uchimura, A. P. Paulikas, V. Stamenkovic and N. M. Markovic, *Science*, 2011, **334**, 1256-1260.
40. W. Tang, E. Sanville and G. Henkelman, *J Phys-Condens Mat*, 2009, **21**, 084204.